Inorg. Chem. **2008**, *47*, 11688−11697

Electronic Structure of a Binuclear Nickel Complex of Relevance to [NiFe] Hydrogenase

Maurice van Gastel,*,† Jennifer L. Shaw,†,‡ Alexander J. Blake,‡ Marco Flores,† Martin Schröder,*,‡ Jonathan McMaster,‡ and Wolfgang Lubitz*,†

Max-Planck-Institut für Bioanorganische Chemie, Stiftstrasse 34-36, D-45470 Mülheim an der Ruhr, Germany, and School of Chemistry, The University of Nottingham, Nottingham, UK NG7 2RD, U.K.

Received July 23, 2008

The binuclear complex $[Ni_2(L)(MeCN)_2]^{3+}$ (L^{2-} = compartmental macrocycle incorporating imine N and thiolate S donors) has a Ni^{III} center bridged via two thiolate S-donors to a diamagnetic Ni^{II} center. The ground-state has dominant $3d_{z^2}$ character similar to that observed for [NiFe] hydrogenases in which Ni^{III} is bridged via two thiolate donors to a diamagnetic center (Fe^{II}). The system has been studied by X-ray crystallography and pulse EPR, ESEEM, and ENDOR spectroscopy in order to determine the extent of spin-delocalization onto the macrocycle L^{2-}. The hyperfine coupling constants of six nitrogen atoms have been identified and divided into three sets of two equivalent nitrogens. The most strongly coupled nitrogen atoms ($a_{iso} \sim 53$ MHz) stem from axially bound solvent acetonitrile molecules. The two macrocycle nitrogens on the Ni^{III} side have a coupling of $a_{iso} \sim 11$ MHz, and those on the Ni^{II} side have a coupling of $a_{iso} \sim 1-2$ MHz. Density functional theory (DFT) calculations confirm this assignment, while comparison of the calculated and experimental ^{14}N hyperfine coupling constants yields a complete picture of the electron-spin density distribution. In total, 91% spin density is found at the Ni^{III} of which 72% is in the $3d_{z^2}$ orbital and 16% in the $3d_{xy}$ orbital. The Ni^{II} contains −3.5% spin density, and 7.5% spin density is found at the axial MeCN ligands. In analogy to hydrogenases, it becomes apparent that binding of a substrate to Ni at the axial positions causes a redistribution of the electron charge and spin density, and this redistribution polarizes the chemical bonds of the axial ligand. For [NiFe] hydrogenases this implies that the H_2 bond becomes polarized upon binding of the substrate, which may facilitate its heterolytic splitting.

Introduction

Hydrogenase enzymes are highly efficient hydrogen-processing catalysts that rely on economically attractive base metals.[1] The [NiFe] hydrogenases mediate hydrogen production and consumption (eq 1), and the active site of these enzymes (Figure 1) comprises a heterobinuclear center incorporating Ni and Fe ions.[2−6] The Fe center is coordinated to three diatomic ligands which have been identified by FTIR studies as two CN^- ligands and one CO.[7−10] The Ni and Fe centers are bridged by S atoms from cysteine residues and,

* To whom correspondence should be addressed. E-mail: vgastel@mpi-muelheim.mpg.de (M.v.G.); m.schroder@nottingham.ac.uk (M.S.); lubitz@mpi-muelheim.mpg.de (W.L.). Tel: +49 (0)208 3063555 (M.v.G.); +44 (0)115 9513490 (M.S.); +49 (0)208 3063614 (W.L.). Fax: +49 (0)208 3063951 (M.v.G.); +44 (0)115 9513563 (M.S.); +49 (0)208 306 3955 (W.L.).

† Max-Planck-Institut für Bioanorganische Chemie.

‡ The University of Nottingham.

(1) Fontecilla-Camps, J. C.; Volbeda, A.; Cavazza, C.; Nicolet, Y. *Chem. Rev.* **2007**, *107*, 5411–5411.

(2) Volbeda, A.; Charon, M.-H.; Hatchikian, E. C.; Frey, M.; Fontecilla-Camps, J. C. *Nature* **1995**, *373*, 580–587.

(3) Higuchi, Y.; Yasuoka, N.; Kakudo, M.; Katsube, Y.; Yagi, T.; Inokuchi, H. *J. Biol. Chem.* **1987**, *262*, 2823–2825.

(4) Fontecilla-Camps, J. C. *J. Biol. Inorg. Chem.* **1996**, *1*, 91–98.

(5) Volbeda, A.; Fontecilla-Camps, J. C. *Coord. Chem. Rev.* **2005**, *249*, 1609–1619.

(6) van Gastel, M.; Lubitz, W. In *High Resolution EPR: Applications to metalloenzymes and metals in medicine*; Hanson, G. R., Berliner, R. J., Eds.; Kluwer Academic: New York, 2008; pp 441−470.

(7) Happe, R. P.; Roseboom, W.; Pierik, A. J.; Albracht, S. P. J.; Bagley, K. A. *Nature* **1997**, *385*, 126–126.

(8) Bleijlevens, B.; van Broekhuizen, F.; De Lacey, A. L.; Roseboom, W.; Fernandez, V. M.; Albracht, S. P. J. *J. Biol. Inorg. Chem.* **2004**, *9*, 743–752.

(9) De Lacey, A. L.; Hatchikian, E. C.; Volbeda, A.; Frey, M.; Fontecilla-Camps, J. C.; Fernandez, V. M. *J. Am. Chem. Soc.* **1997**, *119*, 7181–7189.

(10) Fichtner, C.; Laurich, C.; Bothe, E.; Lubitz, W. *Biochemistry* **2006**, *45*, 9706–9716.

10.1021/ic801383x CCC: $40.75
Published on Web 11/08/2008

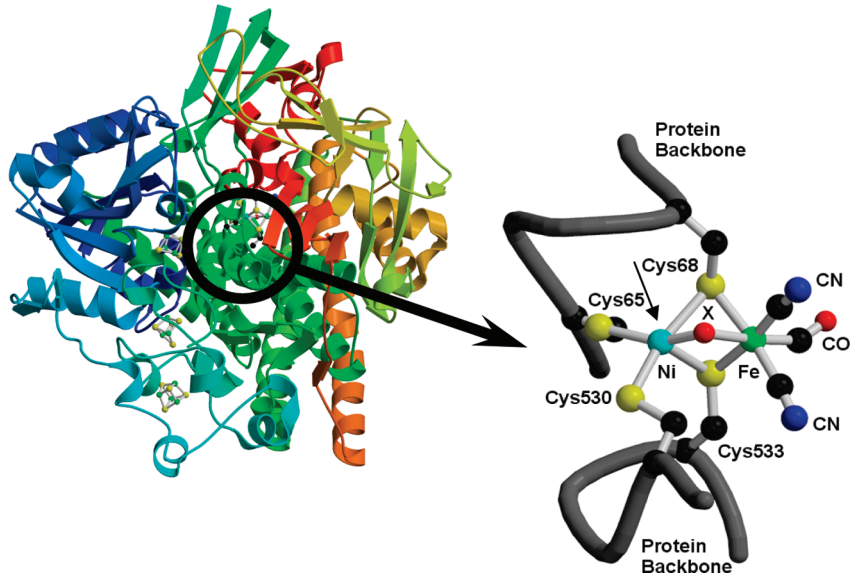

Figure 1. X-ray structure of a [NiFe] hydrogenase (left). The active site of [NiFe] hydrogenases (right). The catalytic activity is believed to occur at the open coordination site of Ni, indicated with an arrow.[20]

in the oxidized inactive form, by an additional species (X), which contains oxygen.[2,11−15] The Ni center is coordinated to two further S atoms from cysteine residues (Figure 1). Although there are subtle differences in the composition of the ligands in the metal centers of the catalytically active [NiFe] hydrogenases from different bacteria (e.g., in some species a selenocysteine is present instead of cysteine), the basic structure is conserved.[16]

$$2H^+ + 2e^- \rightleftharpoons H_2 \qquad (1)$$

During the catalytic cycle the enzyme passes through several redox states. Thirteen states have now been identified,[8] seven of which appear to be physiologically relevant with three involved directly in catalytic activity. It is understood that in the catalytic cycle of [NiFe] hydrogenases the Fe center remains in the formal Fe^{II} state whereas the Ni center shuttles between the diamagnetic 2+ and paramagnetic 3+ oxidation states.[17−19] Electron paramagnetic resonance (EPR) studies, therefore, play a key role in understanding the redox chemistry of the active site in [NiFe] hydrogenases.[20] Quantum chemical calculations have shown that the redox chemistry of [NiFe] hydrogenase is not only limited to the Ni center; rather, in the EPR active states, a significant amount of spin density is found on the S-donor of one of the bridging cysteine ligands.[21] The noninnocence of the cysteine ligands is intriguing, and it has been suggested that a possible role of the cysteine ligands is to act as bases to bind protons during the catalytic process.[4,22]

A range of low molecular weight inorganic complexes have been synthesized with the aim of understanding the electronic structure and function of the active site of [NiFe] hydrogenases.[23,24] Excellent model systems have been reported including mononuclear complexes with exclusively sulfur ligation, binuclear complexes with either identical or different metals, and complexes with a variety of coligands.[25−30] A few functional bi- and heteronuclear model complexes have been reported for hydrogen oxidation and proton reduction.[31−36]

(11) Carepo, M.; Tierney, D. L.; Brondino, C. D.; Yang, T. C.; Pamplona, A.; Telser, J.; Moura, I.; Moura, J. J. G.; Hoffman, B. M. *J. Am. Chem. Soc.* **2002**, *124*, 281–286.
(12) Volbeda, A.; Martin, L.; Cavazza, C.; Matho, M.; Faber, B. W.; Roseboom, W.; Albracht, S. P. J.; Garcin, E.; Rousset, M.; Fontecilla-Camps, J. C. *J. Biol. Inorg. Chem.* **2005**, *10*, 239–249.
(13) Ogata, H.; Hirota, S.; Nakahara, A.; Komori, H.; Shibata, N.; Kato, T.; Kano, K.; Higuchi, Y. *Structure* **2005**, *13*, 1635–1642.
(14) van Gastel, M.; Fichtner, C.; Neese, F.; Lubitz, W. *Biochem. Soc. Trans.* **2005**, *33*, 7–11.
(15) van Gastel, M.; Stein, M.; Brecht, M.; Schröder, O.; Lendzian, F.; Bittl, R.; Ogata, H.; Higuchi, Y.; Lubitz, W. *J. Biol. Inorg. Chem.* **2006**, *11*, 41–51.
(16) Halcrow, M. A.; Christou, G. *Chem. Rev.* **1994**, *94*, 2421–2481.
(17) Huyett, J. E.; Carepo, M.; Pamplona, A.; Franco, R.; Moura, I.; Moura, J. J. G.; Hoffman, B. M. *J. Am. Chem. Soc.* **1997**, *119*, 9291–9292.
(18) Evans, D. J.; Pickett, C. J. *Chem. Soc. Rev.* **2003**, *32*, 268–275.
(19) Wang, Q.; Barclay, J. E.; Blake, A. J.; Davies, E. S.; Evans, D. J.; Marr, A. C.; McInnes, E. J. L.; McMaster, J.; Wilson, C.; Schröder, M. *Chem. Eur. J.* **2004**, *10*, 3384–3396.
(20) Lubitz, W.; Reijerse, E.; van Gastel, M. *Chem. Rev.* **2007**, *107*, 4331–4365.
(21) Stein, M.; Lubitz, W. *Phys. Chem. Chem. Phys.* **2001**, *3*, 2668–2675.
(22) Bruschi, M.; Zampella, G.; Fantucci, P.; De Gioia, L. *Coord. Chem. Rev.* **2005**, *249*, 1620–1640.
(23) Marr, A. C.; Spencer, D. J. E.; Schröder, M. *Coord. Chem. Rev.* **2001**, *219*, 1055–1074.
(24) Bouwman, E.; Reedijk, J. *Coord. Chem. Rev.* **2005**, *249*, 1555–1581.
(25) Li, Z. L.; Ohki, Y.; Tatsumi, K. *J. Am. Chem. Soc.* **2005**, *127*, 8950–8951.
(26) Zhu, W. F.; Marr, A. C.; Wang, Q.; Neese, F.; Spencer, D. J. E.; Blake, A. J.; Cooke, P. A.; Wilson, C.; Schröder, M. *Proc. Natl. Acad. Sci. U.S.A.* **2005**, *102*, 18280–18285.
(27) Stenson, P. A.; Marin-Becerra, A.; Wilson, C.; Blake, A. J.; McMaster, J.; Schröder, M. *Chem. Commun.* **2006**, 317–319.
(28) Green, K. N.; Jeffery, S. P.; Reibenspies, J. H.; Darensbourg, M. Y. *J. Am. Chem. Soc.* **2006**, *128*, 6493–6498.
(29) Jeffery, S. P.; Singleton, M. L.; Reibenspies, J. H.; Darensbourg, M. Y. *Inorg. Chem.* **2007**, *46*, 179–185.
(30) Rampersad, M. V.; Jeffery, S. P.; Golden, M. L.; Lee, J.; Reibenspies, J. H.; Darensbourg, D. J.; Darensbourg, M. Y. *J. Am. Chem. Soc.* **2005**, *127*, 17323–17334.
(31) Matsumoto, T.; Nakaya, Y.; Itakura, N.; Tatsumi, K. *J. Am. Chem. Soc.* **2008**, *130*, 2458–2459.
(32) Ogo, S.; Kabe, R.; Uehara, K.; Kure, B.; Nishimura, T.; Menon, S. C.; Harada, R.; Fukuzumi, S.; Higuchi, Y.; Ohhara, T.; Tamada, T.; Kuroki, R. *Science* **2007**, *316*, 585–587.

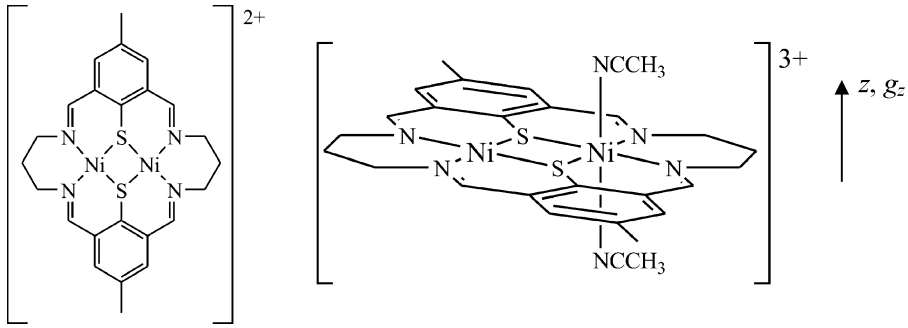

Figure 2. Structures of $[Ni_2(L)]^{2+}$ and $[Ni_2(L)(MeCN)_2]^{3+}$. The g_z and molecular z axes are parallel to the N(MeCN)-Ni directions of the local octahedron at the Ni^{III} center as indicated by an arrow. In the latter complex, the formal valence states of the metals are Ni^{II} and Ni^{III}. For simplicity, both resonance structures, which have a folded conformation, are drawn planar. The folded structures are given in Figures 3 and 8.

To further investigate the degree of delocalization of spin density over Ni and its ligands in a Ni^{III} system in a low molecular weight model, we decided to study the binuclear complex $[Ni_2(L)]^{2+}$ (Figure 2)[37,38] by pulsed EPR, electron nuclear double resonance (ENDOR), electron spin echo envelope modulation (ESEEM), and density functional theory (DFT) calculations. The oxidized complex cation $[Ni_2(L)(MeCN)_2]^{3+}$, formed by one-electron oxidation of $[Ni_2(L)]^{2+}$ in MeCN, is a valence-localized Ni^{II}/Ni^{III} system characterized by optical absorption bands at 510 and 865 nm and g values at 2.035 (g_z), 2.187 (g_y), and 2.202 (g_x).[39] The macrocycle $[L]^{2-}$ is symmetric and nonplanar and contains two metal binding sites. These each comprise two terminal N and two bridging thiolate groups. Though the complex $[Ni_2(L)(MeCN)_2]^{3+}$ does not accurately mimic the geometric structure of [NiFe] hydrogenases, its electronic structure, as expressed by the g values, is similar to the Ni−A, Ni−B, Ni−C, and Ni−L paramagnetic intermediate states of hydrogenase.[20] Initial studies by multifrequency EPR spectroscopy have shown that $[Ni_2(L)(MeCN)_2]^{3+}$ displays a well-resolved pentet structure in the g_z region with a 1:2:3:2:1 intensity distribution, which was attributed to the ^{14}N hyperfine interaction of solvent MeCN ligands in the axial positions.[39] Most probably, the binding of axial solvent molecules contributes substantially to the localized-valence Ni^{II}/Ni^{III} character of the system. Owing to the folded nature of the macrocycle on coordination, it is not sterically possible for both metals to possess two axially coordinated solvent molecules coordinated in a symmetric fashion. The 3d orbitals of the Ni center with two axial ligands are more destabilized than those of the other metal, resulting in the localized-valence nature of the system. The redox potentials observed for hydrogenase are also compatible with a Ni^{II}/Ni^{III} redox couple in the presence of electron-rich, polarizable anionic sulfur ligands that stabilize the Ni^{III} form.[4,40−42]

By studying $[Ni_2(L)(MeCN)_2]^{3+}$ samples enriched with ^{61}Ni ($I = 3/2$) at various microwave frequencies, the ^{61}Ni hyperfine interactions ($|A_x| = 51$ MHz, $|A_y| = 48$ MHz, and $|A_z| = 57$ MHz)[39] have been determined. These hyperfine couplings allow an estimation of the amount of Ni character in the singly occupied molecular orbital (SOMO).[39] However, the remaining part of the SOMO has yet to be identified. We report herein further investigations of the spin density distribution in $[Ni_2(L)(MeCN)_2]^{3+}$ by pulsed EPR spectroscopy and related techniques, in order to provide a complete description of the SOMO and to provide further insight into and to learn more about the mechanism of heterolytic dihydrogen splitting in [NiFe] hydrogenases.

Experimental Section

Perchlorate salts can be explosive if dry. Care was taken in the synthesis of the perchlorate salts described below not to evaporate to dryness or heat any solid formed.

Preparation of Complexes. $[Ni_2(L)](NO_3)_2$. $[Ni_2(L)](NO_3)_2$ was synthesized via an adaptation of the literature method.[37,38,43] 2,6-Diformyl-4-methyl-*N*,*N*-dimethylcarbamylthiophenol (510 mg, 2.03 mmol) was dissolved in *iso*-propanol (150 cm^3) and heated to reflux under N_2. NaOH (80 mg, 2.0 mmol) was added to the refluxing solution which underwent a color change from yellow to dark red. The solution was heated to reflux for 5 h before $Ni(NO_3)_2 \cdot 6H_2O$ (589 mg, 2.03 mmol) and $H_2N(CH_2)_3NH_2$ (0.17 cm^3, 2.03 mmol) were added. The solution was heated to reflux for a further 4 h and filtered while still hot. The red solid was collected and recrystallized from MeCN and Et_2O to give a dark red microcrystalline powder. Yield: 212 mg (38%). ^1H NMR (CD_3NO_2) δ/ppm: 8.02 (s, 4H), 7.56 (s, 4H), 4.42 (t, 4H), 3.83 (d, 4H), 2.38 (s, 6H), 2.10 (d, 2H), 1.80 (q, 2H). ES MS *m*/*z*: 275 ($[M]^{2+}$), 549 ($[M - H]^+$).

$[Ni_2(L)(BF_4)_2]$. Crude $[Ni_2(L)](NO_3)_2$ (212 mg, 314 mmol) obtained in the previous reaction was purified by Soxhlet extraction into MeCN (350 cm^3). At the same time, anion metathesis was carried out by heating the solution to reflux with an excess of Bu_4NBF_4 (616 mg, 785 mmol). The product formed as red crystals

(33) Mealli, C.; Rauchfuss, T. B. *Angew. Chem., Int. Ed.* **2007**, *46*, 8942–8944.
(34) Justice, A. K.; Linck, R. C.; Rauchfuss, T. B.; Wilson, S. R. *J. Am. Chem. Soc.* **2004**, *126*, 13214–13215.
(35) Sellmann, D.; Lauderbach, F.; Geipel, F.; Heinemann, F. W.; Moll, M. *Angew. Chem., Int. Ed.* **2004**, *43*, 3141–3144.
(36) Perra, A.; Davies, E. S.; Hyde, J. R.; Wang, Q.; McMaster, J.; Schröder, M. *Chem. Commun.* **2006**, 1103–1105.
(37) Atkins, A. J.; Black, D.; Blake, A. J.; Marin-Becerra, A.; Parsons, S.; Ruiz-Ramirez, L.; Schröder, M. *Chem. Commun.* **1996**, 457–464.
(38) Atkins, A. J.; Blake, A. J.; Schröder, M. *J. Chem. Soc. Chem. Comm.* **1993**, 1662–1665.
(39) Branscombe, N. D. J.; Atkins, A. J.; Marin-Becerra, A.; McInnes, E. J. L.; Mabbs, F. E.; McMaster, J.; Schröder, M. *Chem. Commun.* **2003**, 1098–1099.
(40) Blake, A. J.; Gould, R. O.; Halcrow, M. A.; Holder, A. J.; Hyde, T. I.; Schröder, M. *J. Chem. Soc., Dalton Trans.* **1992**, 3427–3431.
(41) Fox, S.; Wang, Y.; Silver, A.; Millar, M. *J. Am. Chem. Soc.* **1990**, *112*, 3218–3220.
(42) Kruger, H. J.; Peng, G.; Holm, R. H. *Inorg. Chem.* **1991**, *30*, 734–742.
(43) Brooker, S.; Croucher, P. D.; Roxburgh, F. M. *J. Chem. Soc., Dalton Trans.* **1996**, 3031–3037.

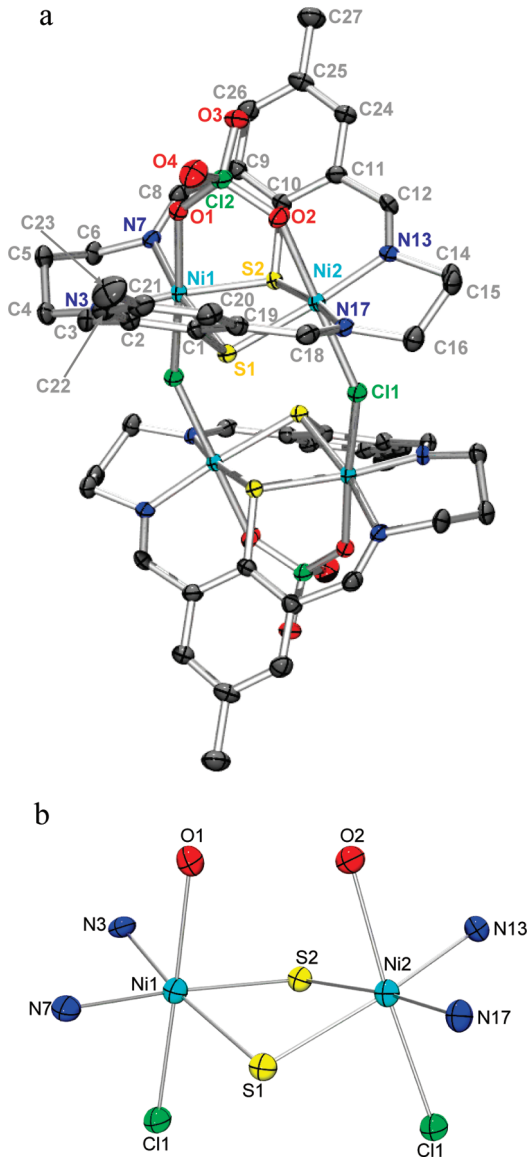

Figure 3. (a) View of $[(Ni_2(L)ClO_4)_2(\mu_2\text{-}Cl)_2]^{x+}$ ($x = 0-2$) as displacement ellipsoid plots at 50% probability. H atoms are omitted for clarity. (b) Coordination geometry of the Ni centers. Labels of the atoms are given in the figure and details of the structure are given in the Supporting Information.

upon the addition of Et_2O to the cooled reaction mixture. The crystal structure of $[Ni_2(L)(PF_6)_2]$ has been reported in ref 38. Yield: 189 mg (83%),. ^{1}H NMR (CD_3NO_2) δ/ppm: 8.20 (s, 4H), 7.57 (s, 4H), 4.44 (t, 4H), 4.09 (d, 4H), 2.38 (s, 6H), 2.10 (d, 2H), 1.80 (q, 2H). IR (KBr) $\tilde{\nu}_{max}/cm^{-1}$: 2972m (C−H stretch), 2894m (C−H stretch), 1627w (C=N stretch), 1556w, 1331s, 1051s (B−F stretch), 887m, 825m.

$[Ni_2(L)(MeCN)_2]^{3+}$. A portion of $[Ni_2(L)](BF_4)_2$ was dissolved in analytical grade MeCN (Merck) and oxidized by addition of $HClO_4$ (70%). The final concentration was ca. 1 mM.

$[(Ni_2(L)ClO_4)_2(\mu_2\text{-}Cl)_2]^{x+}$ ($x = 0-2$). Single crystals of $[(Ni_2(L)ClO_4)_2(\mu_2\text{-}Cl)_2]^{x+}$ ($x = 0-2$) were obtained by adding $HClO_4$ (70%) to dark red crystals of $[Ni_2(L)](BF_4)_2$. Care was taken not to dissolve the crystals. Very dark green crystals, which were unstable except in acidic media, were obtained after one week. These were the only crystallizable oxidation products obtained from a series of oxidation experiments. Unfortunately, under the experimental conditions, additional measurements to determine the charge balance within the unit cell were not feasible, and consequently, the value of x could not be established with certainty.

Crystal Structure Determination. Diffraction data were measured at 150 K as ω scans using Mo Kα radiation (0.71073 Å). The structure was solved by direct methods using SHELXS, and full-matrix least-squares refinements on F^2 were carried out using SHELXL. The hydrogen atoms of the water molecules O29−O36 were not located, but they are included in the unit cell contents and in all parameters derived from them. Computer programs used are as follows: Bruker SMART, Bruker SAINT, and Bruker SHELXTL (Bruker AXS Inc., Madison, WI, 2001); SHELXS97;[44] SHELXL97;[45] enCIFer;[46] and PLATON.[47] The data for the crystal and structural refinement are given in Table S1, Supporting Information.

EPR, ENDOR, and ESEEM. Continuous wave EPR spectra were recorded on a 9 GHz Bruker Elexsys 500E spectrometer with a rectangular 4102ST cavity and an Oxford ESR910 flow cryostat. The temperature was 110 K, microwave frequency 9.639 GHz, microwave power 2 mW, and modulation amplitude 5 G. Q-band pulsed EPR and Davis ENDOR experiments were performed at $T = 10$ K on a Bruker Elexsys FT-EPR system at 34 GHz and a home-built ENDOR cavity. In the Davis ENDOR experiments, the first π pulse had a length of 100 ns corresponding to an excitation bandwidth of 0.18 mT, and the length of the RF pulse was 18 μs. A Hahn echo detection sequence of 40−400−80 ns was used for the ENDOR experiment. The cw EPR spectra were simulated by a home written program made available by Prof. F. Neese. The procedure used for simulation of the ENDOR spectra was adapted from an ESEEM simulation procedure described previously.[48] The bands in the frequency histogram are dressed with a Gaussian function with a width of 1.7 MHz.

X-band 3 pulse ESEEM and Davies ENDOR spectra were measured on a Bruker Elexsys E580 spectrometer in a dielectric ring resonator (ESP 380−1052 DL Q-H) using an Oxford CF935 flow cryostat. The 3 pulse ESEEM experiments were recorded at $T = 10$ K and $\nu_{mw} = 9.708$ GHz; the $\pi/2$ microwave pulses of the $\pi/2-\tau-\pi/2-t-\pi/2-\tau-$echo sequence had a length of 16 ns, and the time τ was 144 ns. After subtraction of the T_1 echo decay, the modulation pattern was multiplied with a Hamming window function, zero-filled to 1024 points and Fourier transformed to the frequency domain. The depicted ESEEM spectra presented are magnitude spectra. Davies ENDOR spectra were recorded with a $\pi-\pi_{RF}-\pi/2-\tau-\pi-$echo sequence. The length of the RF pulse was 10 μs, and the time τ was 400 ns. In this sequence, the length of the π pulse was 112 ns.

In ENDOR as well as ESEEM spectroscopy, two signals are expected for a spin 1/2 nucleus (e.g., ^{1}H). If a_{eff} is the effective hyperfine coupling constant and ν_Z is the Zeeman frequency, then these signals occur at[49]

$$\nu_Z \pm \frac{a_{eff}}{2} \qquad (2)$$

for weakly coupling nuclei with $\nu_Z > a_{eff}/2$ or

(44) Sheldrick, G. M. *Acta Crystallogr., Sect. A* **1990**, *46*, 467–473.
(45) Sheldrick, G. M. *SHELXL-97*; Universtiy of Göttingen: Göttingen, Germany, 1997.
(46) Allen, F. H.; Johnson, O.; Shields, G. P.; Smith, B. R.; Towler, M. *J. Appl. Crystallogr.* **2004**, *37*, 335–338.
(47) Spek, A. L. *J. Appl. Crystallogr.* **2003**, *36*, 7–13.
(48) van Gastel, M.; Coremans, J. W. A.; Jeuken, L. J. C.; Canters, G. W.; Groenen, E. J. J. *J. Phys. Chem. A* **1998**, *102*, 4462–4470.
(49) Schweiger, A; Jeschke, G. *Principles of Pulse Electron Paramagnetic Resonance*; Oxford University Press: Oxford, 2001.

$$\frac{a_{\mathrm{eff}}}{2} \pm \nu_{\mathrm{Z}} \tag{3}$$

for strongly coupled nuclei with $\nu_{\mathrm{Z}} < a_{\mathrm{eff}}/2$. In case of nuclei with spin $I > 1/2$ (e.g., ^{14}N, $I = 1$) additional splitting of each of these signals into two may occur owing to the presence of nuclear quadrupole interaction. In the case of a small quadrupole interaction, $P_{\mathrm{eff}} < \nu_{\mathrm{Z}}$, $a_{\mathrm{eff}}/2$, the equations have to be modified by an additional term[49]

$$\pm 3P_{\mathrm{eff}} \tag{4}$$

For nitrogen atoms for which $\nu_{\mathrm{Z}} \approx a_{\mathrm{eff}}/2$, for example, for the weakly coupled nitrogen atoms (vide infra), the nuclear hyperfine interaction and Zeeman interaction cancel each other in one M_S manifold.[50] Then in the ESEEM spectra, three relatively sharp signals occur at

$$\nu_{\pm} = \frac{P_z}{2}(3 \pm \eta), \quad \nu_0 = P_z\eta \tag{5}$$

where the asymmetry parameter η is defined as[49]

$$\eta = \frac{P_x - P_y}{P_z} \tag{6}$$

Of the other M_S manifold, only the double quantum ($\Delta M_I = 2$) transition is observed at a frequency[49]

$$\nu_{\mathrm{dq}} = 2\left[\left(\frac{a_{\mathrm{eff}}}{2} + \nu_n\right)^2 + \left(\frac{P_{\mathrm{eff}}}{2}(3 + \eta^2)\right)^2\right]^{1/2} \tag{7}$$

Density Functional Theory (DFT) Studies. DFT calculations were performed using the ORCA program.[51] The complex $[Ni_2(L)(MeCN)_2]^{3+}$ (Figure 2) incorporating two axially coordinated MeCN molecules bound to the Ni^{III} center only was used as the model geometry. The coordinates are given in Supporting Information. The calculations used the B3LYP functional and a spin-unrestricted formalism. For light atoms the iglo-iii basis set of Kutzelnigg et al.[52] was used, while for Ni the "cp" basis set[53] was used augmented with two polarization functions[54] and one diffuse function. Hyperfine coupling constants were calculated in a coupled-perturbed SCF formalism. Convergence criteria were 10^{-6} Eh for the change in energy and 10^{-5} and 10^{-6} for the average and maximum change in the electron density, respectively. In spin-unrestricted calculations, negative spin density may arise as a result of spin polarization. Spin polarization occurs because the exchange interaction only occurs between electrons of equal spin. This means that the two electrons of each electron pair have a different interaction with the unpaired electron. The slight inequivalence of the two electrons within the pair causes their wave functions to be slightly different, thus introducing small additional positive and negative spin density.

In order to investigate the effect of polarization of the H_2 bond upon binding to Ni in the active site of [NiFe] hydrogenase, three additional calculations have been performed. The first involves a calculation of $[Ni_2(L)(MeCN)(H_2)]^{3+}$, where one of the MeCN ligands has been replaced by H_2. Since the Ni atom in hydrogenase is five coordinate with four S and one O coordination and has one open coordination site for H_2, the second model consisted of $[Ni^{3+}(SH^-)_4(OH^-)(H_2)]$. The third model takes into account the complete active site of hydrogenase. A pictorial representation of all three systems is included in the Supporting Information.

Results and Discussion

Crystal Structure. The crystal structure of $[(Ni_2(L)ClO_4)_2(\mu_2\text{-}Cl)_2]_2(ClO_4)_{12}\cdot 15H_2O$ confirms that a tetranuclear species forms from two $[Ni_2(L)]$ units bridged by two chloride ions, with the Ni centers in each edge-sharing bioctahedral $[Ni_2(L)]$ unit bridged by a perchlorate anion. The asymmetric unit comprises half of the tetranuclear complex cation with the other half generated by inversion. Each Ni ion is six coordinate and bound to two nitrogen atoms and two sulfur atoms of the macrocycle, a bridging chloride ion, and an oxygen atom from a bridging perchlorate anion (Figure 3). The Ni−N bond lengths are 1.949(5), 1.946(5), 1.960(4), and 1.961(4) Å, and the the Ni−S bond lengths are 2.2372(15), 2.2380(15), 2.2345(15), and 2.2405(15) Å. These bond lengths are significantly longer than those observed for the square planar $Ni^{II}Ni^{II}$ species $[Ni(L)](PF_6)_2\cdot 2DMF$ where the Ni−N bond lengths are 1.927(15) and 1.906(15) Å and the Ni−S bond lengths are 2.181(6) and 2.171(6) Å.[38] The Ni−Cl bond lengths are 2.4060(15) and 2.3991(15) Å and the Ni−O bond lengths are 2.185(4) and 2.211(4) Å.

It was not possible to assign formal oxidation states of Ni based on the stoichiometry of the complex as there are six additional perchlorate counteranions per tetranuclear fragment identified in the crystal structure. Due to the difficulty of accurately locating H atoms in a crystal structure, the exact charge of the complex is not known. An assignment to Ni^{III} is favored based on the bond lengths. A search of the literature resulted in the identification of just three six-coordinate Ni^{III} complexes with at least one S donor.[40,55,56] In these complexes the average Ni^{III}−S bond lengths are 2.31, 2.37, and 2.28 Å, respectively. The last value in particular corresponds well to the average Ni−S bond length of 2.238(4) Å in $[(Ni_2(L)ClO_4)_2(\mu_2\text{-}Cl)_2]_2(ClO_4)_{12}\cdot 15H_2O$.

EPR Spectroscopy. The continuous wave (cw) EPR spectrum of a frozen solution of $[Ni_2(L)(MeCN)_2]^{3+}$ formed by the oxidation of $[Ni_2(L)]^{2+}$ with $HClO_4$ in MeCN is shown in Figure 4. The spectrum is almost axially symmetric and is virtually identical to that reported previously.[39] At the high-field side of the spectrum (g_z), a hyperfine structure of five bands in a 1:2:3:2:1 intensity ratio is present, indicative of coupling to two equivalent nitrogen atoms. The spectrum is simulated with g values of $g_x = 2.205$, $g_y = 2.195$, and $g_z = 2.040$, compatible with the $3d_{z^2}^1$ ground-state of Ni^{III}, and a set of hyperfine coupling constants of $A_x = 50.4$ MHz, $A_y = 51.8$ MHz, and $A_z = 57.9$ MHz for the two equivalent nitrogen atoms with $I = 1$ (values determined from simulation of ENDOR spectra, vide infra). Contributions from other nuclei that do not give rise to resolved hyperfine structure

(50) Flanagan, H. L.; Singel, D. J. *J. Chem. Phys.* **1987**, *87*, 5606–5616.
(51) Neese, F. *ORCA*, An ab initio, Density Functional and Semiempirical program package, Version 2.5; University of Bonn, 2006.
(52) Kutzelnigg, W.; Fleischer, U.; Schindler, M. *NMR Basic Principles and Progress*; Springer-Verlag: Heidelberg, 1991.
(53) Neese, F. *Inorg. Chim. Acta* **2002**, *337C*, 181–192.
(54) Wachters, A. J. *J. Chem. Phys.* **1970**, *52*, 1033–1036.
(55) Garner, M.; Lewinski, K.; Pattek-Janczyk, A.; Reglinski, J.; Sieklucka, B.; Spicer, M. D.; Szaleniec, M. *Dalton Trans.* **2003**, 1181–1185.
(56) Kersting, B.; Siebert, D. *Inorg. Chem.* **1998**, *37*, 3820–3828.

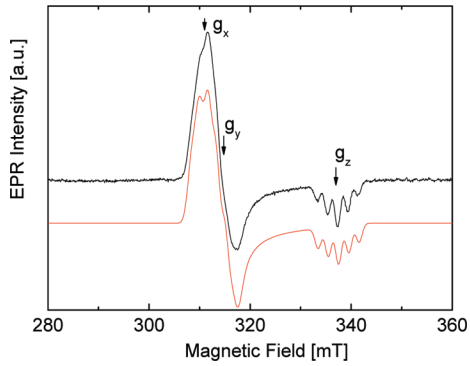

Figure 4. Continuous wave EPR spectrum of $[Ni_2(L)(MeCN)_2]^{3+}$ formed by oxidation of $[Ni_2(L)](BF_4)_2$ by $HClO_4$ in MeCN. Black: experimental spectrum. Red: simulation. Experimental conditions: $T = 110$ K, $\nu = 9.639$ GHz, $P_{mw} = 2$ mW, modulation amplitude 0.5 mT. Simulation parameters: $g_x = 2.205$, $g_y = 2.195$, and $g_z = 2.040$, linewidths $w_x = 0.92$ mT, $w_y = 0.94$ mT, and $w_z = 0.71$ mT, nitrogen hyperfine couplings $A_x = 50.4$ MHz, $A_y = 51.8$ MHz, and $A_z = 57.9$ MHz.

are included in the three line width parameters $w_x = 0.92$ mT, $w_y = 0.94$ mT, and $w_z = 0.71$ mT.

ENDOR Spectroscopy. In Figure 5 (top), the Q-band Davis ENDOR spectrum for $[Ni_2(L)(MeCN)_2]^{3+}$ (0−60 MHz) is shown. It encompasses resonances from the protons around the ^{1}H Zeeman frequency at about 47 MHz. Furthermore, resonances from a large ^{14}N coupling spaced around $A^{(1)}/2$ separated by $2\nu(^{14}N)$ are observed and a resonance at ∼8.5 MHz that belongs to ^{14}N of the macrocyclic ligand.

Strongly Coupled Nitrogen Atoms. Orientation-selected Q-band Davies ENDOR spectra between 12 and 40 MHz are shown in Figure 5 (bottom). A set of four signals between 20 and 35 MHz is observed. The difference in frequency of bands one and three and two and four (counted from left to right, see Figure 5) is equal to twice the Zeeman frequency of ^{14}N in all of the spectra, indicating that these signals originate from nitrogen that is strongly coupled to the electron spin ($|a_{eff}|/2 > \nu_N$). The hyperfine coupling constant can be read from the center of the four bands and varies slightly over the magnetic field range ($|a_{eff}|/2 \approx 25-29$ MHz). The additional splitting of the ENDOR lines is caused by the ^{14}N quadrupole interaction (see Experimental Section). At high magnetic field (effective g value 2.037, cf. Figure 5) the hyperfine coupling constant is identical to that obtained from the EPR spectrum and, therefore, the structure of the four bands in the ENDOR spectra stems from the same two strongly coupled nitrogen atoms as those responsible for the hyperfine splitting in the EPR spectrum.

Simulations of the ENDOR spectra are included in Figure 5, and optimized nuclear hyperfine and quadrupole parameters are given in Table 1. The simulations in which only the electron Zeeman interaction is considered for the orientation selection procedure reproduce the positions of the four experimentally observed bands very well and give reasonable agreement for their intensities. The hyperfine interaction is dominantly isotropic ($a_{iso} = +53.4$ MHz) with minor anisotropy ($A_x' = -3.0$ MHz, $A_y' = -1.6$ MHz, $A_z' = +4.5$ MHz) with an angle of 6° between the A_z' and g_z principal axes. The large value for a_{iso} as well as the small angle between the A_z' and g_z axes indicates that the ^{14}N nuclei are bound axially to Ni^{III} and have a large overlap with the SOMO, which is dominated by the $3d_{z^2}$ orbital. The nuclear quadrupole splitting P can obtained from the observed splitting of each pair of spectral lines (cf., for example, Figure 5, spectrum at $g_{eff} = 2.037$). The optimized quadrupole parameters e^2qQ/h and η, defined as $e^2qQ/h = 2P_z$, $\eta = (P_x - P_y)/P_z$, amount to −2.58 MHz and 0.12, respectively. For pure MeCN the values from nuclear quadrupole resonance studies[57] are $e^2qQ/h = 3.738$ MHz and $\eta = 0.0046$. Usually, the absolute sign of e^2qQ/h cannot be determined experimentally. However, in this case the nitrogen hyperfine interaction is so large that it is either completely resolved in the EPR spectrum or contributes substantially to the line width (cf. Figure 4). Under such conditions, the electron-spin transition induced by the microwaves becomes hyperfine semiselective, and the sign of the quadrupole splitting can then be deduced.[58] The procedure is described in the Supporting Information, and it turns out that P_z is negative.

Macrocycle Nitrogen Atoms of "Intermediate" Coupling. In addition to the strong signals due to axially bound MeCN, it can be expected that the nitrogen atoms of the macrocycle could also give rise to resonances, albeit with smaller coupling constants that may not be resolved in the EPR spectrum. In order to investigate the delocalization of spin density over the macrocyclic N-donors, Davies ENDOR spectra have been recorded at X-band (9 GHz) microwave frequency and the part of the spectrum between 1 and 10 MHz is displayed in Figure 6. The ENDOR spectra show a rich structure between 4 and 7 MHz, and the observed bands have been simulated by tentatively assuming that they are derived from nitrogen (the assignment is confirmed by DFT calculations and the absolute sign of A and P is inferred from the calculations, vide infra). Simulations are included in red in Figure 6, and the optimized simulation parameters are included in Table 1. The nuclear quadrupole parameters e^2qQ/h and η did not require optimization. The isotropic coupling constant is assessed to be 11.0 MHz, smaller than that for the axial N atoms. Likewise the anisotropic couplings are also smaller, implying a larger effective distance from the unpaired electron. The principal axes A_z' and g_z are almost perpendicular to one another with an angle of 80 ± 10°, and the P_z and g_z principal axes are also almost perpendicular (75 ± 10°). This provides strong evidence that the resonances originate from a nitrogen atom or nitrogen atoms situated in the equatorial plane of the spin-carrying $3d_{z^2}$ orbital, that is, nitrogen atoms of the macrocycle. Since the hyperfine structure for these nitrogen atoms is not resolved in the EPR spectrum, the microwave transitions are not hyperfine selective in this case. The observed agreement between simulation and experiment with respect to signal intensities is better than that for the strongly coupled solvent nitrogen atoms.

(57) Colligiani, A.; Guibe, L.; Haigh, P. J.; Lucken, E. A. C. *Mol. Phys.* **1968**, *14*, 89–97.
(58) Biehl, R.; Lubitz, W.; Möbius, K.; Plato, M. *J. Chem. Phys.* **1977**, *66*, 2074–2078.

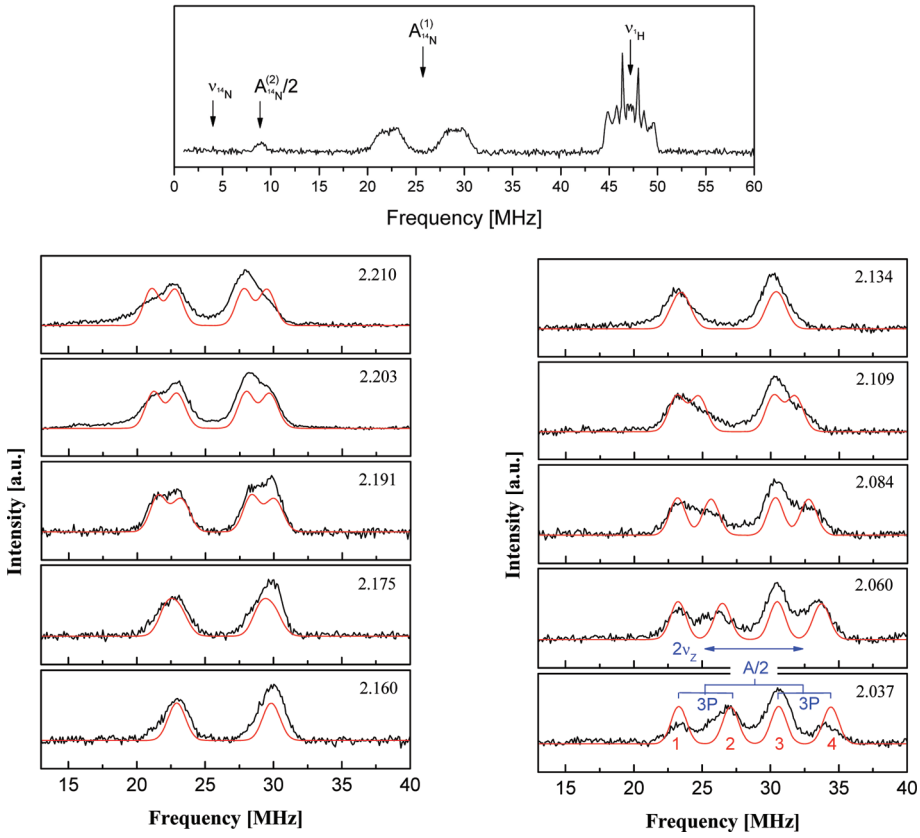

Figure 5. Q-band ESE detected Davies ENDOR spectra of the axially coordinated nitrogens in $[Ni_2(L)(MeCN)_2]^{3+}$. The top spectrum was recorded at 1.1075 T. Signals between 45 and 50 MHz are protons. The effective g values are included in the figure. Black: experimental spectra. Red: simulations. Experimental conditions: $T = 10$ K, $\nu_{mw} = 33.945$ GHz, length of RF pulse 18 μs, length of inversion pulse 100 ns, detection sequence 40−400−80 ns. For simulation parameters, see Table 1. The nuclear Zeeman (ν), hyperfine ($A/2$), and quadrupole splitting (P) are indicated in blue in the spectrum at $g_{eff} = 2.037$.

Table 1. ^{14}N Nuclear Hyperfine and Quadrupole Coupling Constants [MHz] and Angles [deg] of the Respective Principal Axes with the Principal z Axis of the g Tensor for $[Ni_2(L)(MeCN)_2]^{3+}$ As Determined from Simulation of the ENDOR and ESEEM Spectra and DFT Calculations[a]

		hyperfine interaction					quadrupole interaction			
				angle with g_z axis					angle with g_z axis	
		exp	DFT	exp	DFT		exp	DFT	exp	DFT
^{14}N(MeCN)	a_{iso}	+53.4	+67.8			e^2qQ/h	−2.58	−1.93		
						η	0.12	0.03		
	A_x'	−3.0	−2.5	85	b	P_x	+0.72	+0.47	87	88
	A_y'	−1.6	−2.4	90	b	P_y	+0.57	+0.50	90	70
	A_z'	+4.5	+4.9	6	15	P_z	−1.29	−0.97	4	20
^{14}N(Ni^{III})	a_{iso}	+11.0	+16.3			e^2qQ/h	−1.75[c]	−1.75		
						η	0.18	0.18		
	A_x'	−0.5	−1.9	31	34	P_x	+0.36	+0.36	15	27
	A_y'	−1.5	−2.4	61	61	P_y	+0.52	+0.52	90	66
	A_z'	+2.0	+4.3	80	78	P_z	−0.87	−0.87	75	82
^{14}N(Ni^{II})	a_{iso}	−0.4[c]	−0.95			e^2qQ/h	−1.60[c]	−1.60		
						η	0.22	0.19		
	A_x'	+0.13[c]	+0.2	64	68	P_x	+0.31	+0.32	27	38
	A_y'	+0.23[c]	+0.1	26	42	P_y	+0.49	+0.47	68	64
	A_z'	−0.36[c]	−0.4	90	56	P_z	−0.80	−0.80	75	65

[a] In total, two symmetry-equivalent MeCN nitrogens are present, as well as two equivalent macrocycle nitrogens on both the Ni^{III} and Ni^{II} centers. The calculated g values are $g_x = 2.112$, $g_y = 2.100$, and $g_z = 2.025$. Since the g tensor is nearly axial, only the angle with the g_z axis is well defined. The errors of the parameters used in the simulation are principal values ± 0.2 MHz; angles ± 10°. [b] Undefined because of near axiality of the hyperfine tensor. [c] The sign is inferred from the DFT calculation.

ESEEM Experiments. Macrocycle Nitrogen Atoms of Weak Coupling. Since the localized valence $[Ni_2L]^{3+}$ macrocycle contains two sets of two equivalent nitrogen atoms with one set being characterized by ENDOR spectroscopy, electron spin echo envelope modulation (ESEEM) experiments have been performed to investigate the presence of further weakly coupled nitrogen atoms. The ESEEM technique exhibits a better sensitivity than ENDOR in the low-frequency range and is most sensitive to nuclei for which the hyperfine interaction is about equal to the nuclear Zeeman interaction. This phenomenon is called the "exact cancellation condition".[50] The three-pulse ESEEM spectra (frequency domain) recorded at the canonical orientations are shown in Figure 7. Strong signals are observed, and the ESEEM

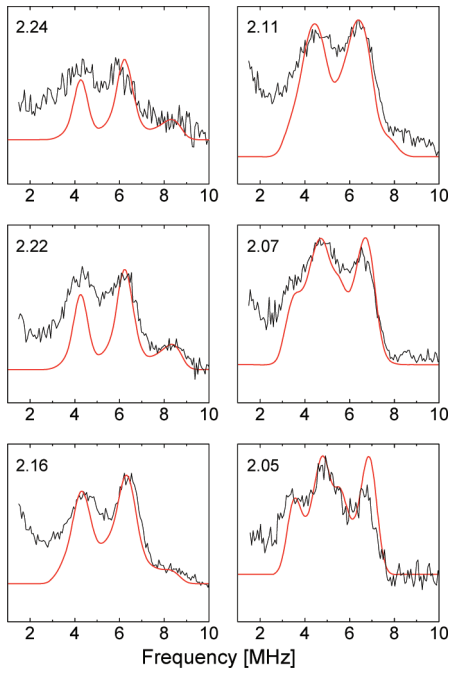

Figure 6. X-band ESE detected Davies ENDOR spectra of the macrocycle nitrogens on the Ni^{III} side in $[Ni_2(L)(MeCN)_2]^{3+}$. Black: experimental spectra. Red: simulations. Experimental conditions: $T = 5$ K, $\nu_{mw} = 9.708$ GHz, length of RF pulse 18 μs, length of inversion pulse 112 ns, detection sequence 56−400−112 ns. The effective g values are included in the figure. Owing to the large line width of the EPR spectrum, ENDOR spectra could be recorded at an effective g value larger than 2.205.

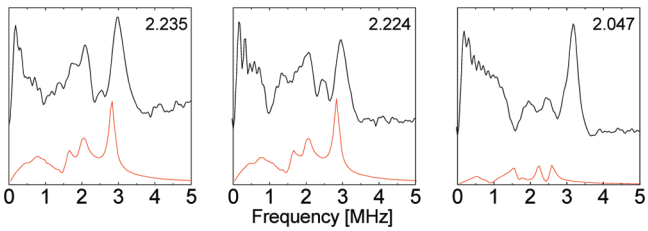

Figure 7. X-band 3-pulse ^{14}N ESEEM spectra of $[Ni_2(L)(MeCN)_2]^{3+}$. Experimental conditions: $T = 10$ K, $\nu_{mw} = 9.708$ GHz, length of 90° pulses 16 ns, $\tau = 144$ ns. A four step phase cycle was used for acquiring the ESEEM spectra. The signals stem from the macrocycle nitrogen atoms on the Ni^{II} center.

spectra display multiple bands below 4 MHz. The observation of these bands confirms the presence of nitrogen atoms with a weak interaction of about 1 MHz with the unpaired electron.

Attempts have been made to simulate the ESEEM spectra; however, the agreement between experiment and simulation in this case is poor. Though the bands in the spectra at the low-magnetic-field side are reasonably well simulated, the simulation fails to reproduce the strong band at 3.2 MHz in the spectrum at $g = 2.034$. The simulation could not be improved by further optimization of nuclear hyperfine and quadrupole parameters. The reason for this failure is probably that the weak coupling of 1 MHz represents nitrogen nuclei that are located far away from the unpaired electron at positions where the wave function coefficients of the SOMO are small. For such weak couplings, effects caused by heterogeneity of the environment will have a large relative effect on the magnitude of the coupling constants. The

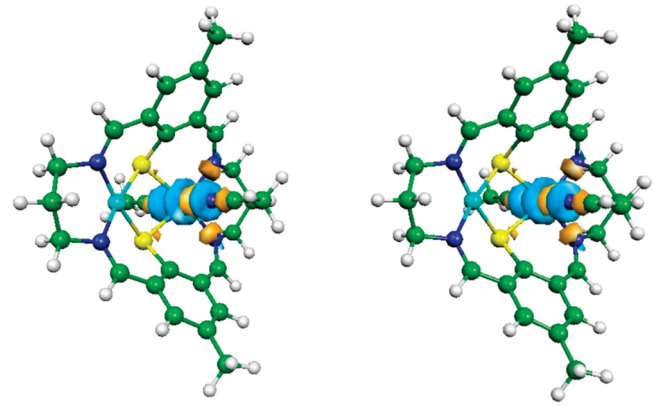

Figure 8. Stereoview of the singly occupied natural orbital, obtained after diagonalization of the electron density matrix of $[Ni_2(L)(MeCN)_2]^{3+}$. The contour of the $3d_{z^2}$ orbital on Ni^{III} can be recognized. Spin density is also present on the nitrogen atoms of the axially coordinating solvent molecules, and a small amount of density is found on the macrocycle. The calculated principal g_z axis is parallel to the C_∞ axis of the $3d_{z^2}$ orbital. The density plot has been created with the program Molekel.

parameters for these nitrogen atoms can, therefore, only be used as an indication of the order-of-magnitude of the couplings. These are included in Table 1 and display very small coupling constants.

The isotropic hyperfine coupling constant is ca. 0.4 MHz indicating the presence of less than 1% spin density at these nitrogen atoms. The quadrupole parameters e^2qQ/h and η are −1.60 MHz and 0.19, respectively, and the A_z' and g_z axis are found to be perpendicular, confirming that the resonances are associated with the macrocyclic nitrogens that lie approximately in the equatorial plane of the $3d_{z^2}$ orbital. Since the coupling constants are smaller by about an order of magnitude compared to the "intermediately coupled" nitrogen atoms, the weakly coupled nitrogen atoms are identified as those of the macrocycle on the Ni^{II} side and the nitrogen atoms of the intermediate coupling as those on the Ni^{III} side.

DFT Calculations. On the basis of the observed pentet pattern in the EPR spectrum, the smallest conceivable model for DFT calculations is comprised of two Ni atoms, the macrocycle L and two MeCN molecules from the solvent (Figure 2) that are both bound axially to one of the two Ni atoms. Because of the nonplanarity of the macrocycle, it is sterically not possible for both Ni atoms to possess a saturated coordination sphere with four axially bound MeCN molecules. After geometry optimization of this model in vacuo, the macrocycle retained its bowl shape. The asymmetry induced by the solvent molecules has a profound effect on the calculated electronic structure. The Mulliken spin density distribution indicates the presence of 91% spin density on the six coordinate Ni center bound by two MeCN ligands (i.e., the Ni^{III} atom) and −3.5% spin density on the other Ni (i.e., the Ni^{II} atom), consistent with the formal Ni^{III}/Ni^{II} character after single oxidation. Each MeCN nitrogen carries ca. 7.5% spin density, the bridging sulfur atoms −2%, each macrocycle nitrogen at the Ni^{III} side 3.8% and those at the Ni^{II} side −0.4% each. It should be noted that the negative spin densities are the result of spin polarization and that the sum of all atomic spin densities equals 100%. The singly

occupied natural orbital is shown in Figure 8, where the contour of the $3d_{z^2}$ orbital at the Ni^{III} center is visible along with the p_z orbitals of the MeCN nitrogens. The g values, calculated with the formalism described previously,[59] gives $g_x = 2.112$, $g_y = 2.100$, $g_z = 2.025$. Comparison with the experimental values of $g_x = 2.205$, $g_y = 2.195$, $g_z = 2.040$ shows that only about 50% of the experimentally observed g shift is reproduced by the calculation, even though the bulk spin density resides on Ni. In this context it should be noted that it is a general problem of the DFT method to accurately reproduce g shifts, which are typically underestimated by about 30%.[59] The calculated principal z axis of the g tensor is parallel to the C_∞ symmetry axis of the $3d_{z^2}$ orbital and perpendicular to the local equatorial plane of the Ni^{III} center.

Surprisingly, the 91% spin density at Ni^{III} is partitioned between the $3d_{z^2}$ orbital (72%) and the $3d_{xy}$ orbital (16%). Within the concepts of crystal field theory the presence of the $3d_{xy}$ orbital in the singly occupied molecular orbital is indeed compatible with an elongated octahedron[6,60,61] and is also in-line with an increased g_z value,[6] according to the expressions

$$\begin{aligned} g_x &= g_e - (6E^2 + 2A^2)\lambda/\Delta_{yz} \\ g_y &= g_e - (6E^2 + 2A^2)\lambda/\Delta_{xz} \\ g_z &= g_e - 8A^2\lambda/\Delta_{x^2-y^2} \end{aligned} \tag{8}$$

where λ is the spin−orbit-coupling parameter for Ni^{III} ($\lambda < 0$), the energy differences of the respective d orbitals with the singly occupied orbital are expressed by Δ, and A and E are the coefficients of the $3d_{xy}$ and $3d_{z^2}$ orbitals in the SOMO, respectively. Note that these expressions have to be modified further when going from crystal field theory to ligand field theory in which the participation of the ligand orbitals in the SOMO is allowed. The presence of ligand orbitals may reduce the metal character in both the SOMO as well as in the lower-lying doubly occupied orbitals that contribute to the g shifts within the perturbation theory formalism.

The presence of 91% spin density is compatible with the experimentally determined ^{61}Ni dipolar hyperfine coupling constants of 71 MHz (23.6×10^{-4} cm^{-1}), −34 MHz (-11.3×10^{-4} cm^{-1}), and −37 MHz (-12.3×10^{-4} cm^{-1}).[39] By using single-ζ Slater functions, the anisotropic hyperfine interaction for a mixed $3d_{xy}$ and $3d_{z^2}$ ground state becomes (see Supporting Information):

$$\vec{A} = -\frac{\mu_0}{4\pi}\gamma_e\gamma_N\left(\frac{\zeta}{a_0}\right)^3\frac{4}{2835} \times \begin{pmatrix} -\frac{1}{2}(A^2 - E^2) & \sqrt{3}AE & 0 \\ \sqrt{3}AE & -\frac{1}{2}(A^2 - E^2) & 0 \\ 0 & 0 & (A^2 - E^2) \end{pmatrix} \tag{9}$$

where $a_0 = 0.52917$Å, μ_0 is the permeability in vacuum, ζ is the Slater exponent, and γ_e and γ_N are the electron and nuclear gyromagnetic ratios. Contributions from spin density at the ligands are neglected. It is noted that the contributions of the spin densities in the $3d_{z^2}$ and $3d_{xy}$ orbitals have opposite signs and partially cancel each other in eq 9. Moreover, in general, rhombicity is introduced for a mixed $3d_{xy}$ and $3d_{z^2}$ ground state. However, an axial tensor may be recovered when $A = \pm\sqrt{3}E$. The principal z axis is unaffected by the admixture of the $3d_{z^2}$ and $3d_{xy}$ orbitals. Diagonalization with $A^2 = 0.16$, $E^2 = 0.72$, and $\zeta = 12.65$[62,63] gives $A_x' = +114$ MHz, $A_y' = -41$ MHz, and $A_z' = -74$ MHz. This simple single-ζ model predicts values that are somewhat too large, an observation that has been made before in other nickel systems.[60] This is not surprising given the fact that the orbital coefficient is optimized for the total energy of the nickel atom; it is rather unlikely that this value is also best for evaluating hyperfine interactions of nickel in coordination complexes.

Comparison between Experimental and Calculated Nitrogen Coupling Constants. In the DFT calculation, three sets of equivalent pairs of nitrogen atoms are found. The calculated nuclear hyperfine and quadrupole constants for these nitrogen atoms are included in Table 1. The strongly coupled axial MeCN nitrogens have a calculated isotropic hyperfine interaction of $a_{iso} = +67.8$ MHz, for the intermediately coupled ring nitrogen atoms of the macrocycle at the Ni^{III} side $a_{iso} = +16.3$ MHz, and for the weakly coupled nitrogen atoms on the Ni^{II} side $a_{iso} = -0.95$ MHz. The experimental values show a similar trend, thus confirming the assignment. A more detailed comparison is given in Table 1. For the axial MeCN nitrogens, the anisotropic coupling constants are also in agreement with experiment, as are the angles of the unique principal axis (A_z') with the g_z principal axis. All calculated nuclear quadrupole parameters of all sets of nitrogen atoms, including the angles of each principal axis with the g_z axis, agree well with experiment.

The largest difference between experiment and theory in this system concerns the hyperfine interaction of the weakly coupled macrocycle nitrogen atoms at the Ni^{II} side. The value for a_{iso} differs by more than a factor of 2, and the experimentally determined and calculated angles with the g_z principal axis also differ substantially. The most likely reason for this discrepancy lies mainly in the small spin density present at these nitrogen atoms (only −0.4%). The heterogeneity of the local environment will cause heterogeneity in the electronic structure, which is, to some extent, amplified by the symmetric nature of the macrocycle. Furthermore, a small redistribution of spin density will then have the largest *relative* effect at those atoms where little spin density is present. Taking into account that the ESEEM effect depends critically and nonlinearly on how well the exact cancelation condition is fulfilled,[20] the poor agreement between the ESEEM spectra and simulation on one side, and also the somewhat mediocre agreement between experiment and theory for the hyperfine couplings is likely rooted in this heterogeneity. The nuclear quadrupole interaction, which is determined by the electric field gradient caused by *all* electrons at nitrogen, is not sensitive to these heterogeneities.

(59) Neese, F. *J. Chem. Phys.* **2001**, *115*, 11080–11096.
(60) Morton, J. R.; Preston, K. F. *J. Chem. Phys.* **1984**, *81*, 5775–5778.
(61) Abragam, A.; Bleaney, B. *Electron Paramagnetic Resonance of Transition Metal Ions*; Oxford University Press: Oxford, 1970.

The calculated and experimental quadrupole parameters for the weakly coupled nitrogen atoms are found to be in good agreement.

Conclusions and Implications for [NiFe] Hydrogenases. The complex $[Ni_2(L)(MeCN)_2]^{3+}$ has been studied by EPR, ENDOR, and ESEEM spectroscopies and DFT calculations. Although the crystal structure of the tetranuclear complex $[(Ni_2(L)ClO_4)_2(\mu_2\text{-}Cl)_2]^{x+}$ ($x = 0-2$) and the solution structure of the binuclear complex $[Ni_2(L)(MeCN)_2]^{3+}$, inferred from spectroscopic studies, are superficially very different, the bowl shaped structure of the macrocycle observed in the X-ray analysis has also been obtained after DFT geometry optimizations for $[Ni_2(L)(MeCN)_2]^{3+}$ and $[Ni_2(L)(MeCN)_2]^{2+}$ in vacuo. It is therefore likely that the solution structure is also bowl shaped. In both the crystal structure as well as in the DFT calculations, oxidized Ni centers are present, though in the former case an assignment of formal oxidation states to the Ni centers was not possible.

The electron-spin density distribution has been investigated by examining the hyperfine coupling constants of nitrogen nuclei magnetically coupled to the unpaired electron, and six nitrogen atoms have been spectroscopically identified. These are divided into three sets of two equivalent nitrogen atoms. The set of strongly coupled nitrogen atoms (a_{iso} = 53.4 MHz) are assigned to the N atoms of the MeCN molecules that are axially bound to Ni^{III}. The set of nitrogen atoms with intermediate coupling (a_{iso} = 11.0 MHz) are assigned to macrocyclic nitrogen atoms directly bound to Ni^{III} in the equatorial plane of the $3d_{z^2}$ orbital. The third set ($a_{iso} = -0.4$ MHz) of coupling constants is assigned to the macrocycle nitrogen atoms at the Ni^{II} side. By comparison with DFT calculations, it can be concluded that the system is a $Ni^{III}-Ni^{II}$ system with localized valences in which 91% electron spin density is found at Ni^{III} and −3.5% at Ni^{II}. The 91% spin density at the Ni^{III} center is partitioned between the $3d_{z^2}$ orbital (72%) and the $3d_{xy}$ orbital (16%). The remaining spin density is delocalized over the macrocycle, −2% at each sulfur atom and 3.8% at the macrocycle nitrogen atoms of Ni^{III}. Owing to the symmetric nature of the macrocycle, the amount of delocalization over the macrocycle changes with heterogeneity of the local environment. This effect is most apparent for the weakly coupled nitrogen atoms at the Ni^{II} side.

With respect to [NiFe] hydrogenase, the presence of 7.5% electron-spin density at each axial ligand is an important finding. It is believed that the site of catalytic activity in [NiFe] hydrogenases is the redox-active Ni center.[6] From the spectroscopic measurements and analysis presented here, it becomes clear that the interaction between Ni^{III} and its axial ligand redistributes some of the electron density away from the ligand and toward the metal center.[64] In this way electron-spin density arises at the ligand and the chemical bonds of the axial ligand become polarized, as is observed in the DFT calculations. This is an important finding and may hint at a mechanism for [NiFe] hydrogenases where the substrate H_2 binds to Ni and the H_2 bond becomes polarized. In order to test the validity of this hypothesis, additional calculations have been performed on a $[Ni_2(L)(MeCN)(H_2)]^{3+}$ molecule where one axial MeCN is artificially replaced by H_2. Indeed, the H_2 bond becomes polarized, even more so than in the case of MeCN, and up to 20% spin density is found on the distal hydrogen atom. Similar effects are observed for more hydrogenase-like systems with $[Ni^{3+}(SH^-)_4(OH^-)(H_2)]$ coordination, where the distal H atom acquires 16% spin density, and in a faithful model of the active site in [NiFe] hydrogenase (see Supporting Information), where 26% spin density is found at the distal H atom. Though this examination does not prove that molecular hydrogen actually binds at the axial position to nickel, if it does, the H_2 bond becomes strongly polarized, which in turn facilitates the heterolytic splitting of H_2.

Acknowledgment. We thank the EPSRC UK and the University of Nottingham for support. M.S. gratefully acknowledges receipt of a Royal Society Wolfson Merit Award and of a Royal Society Leverhulme Trust Senior Research Fellowship. This work was supported by the Max Planck Gesellschaft and by the EU (SolarH2).

Supporting Information Available: Crystallographic Information File (CIF) for $[(Ni_2(L)ClO_4)_2(\mu_2\text{-}Cl)_2]^{x+}$, coordinates of the model for $[Ni_2(L)(MeCN)_2]^{3+}$ used in the DFT calculations, determination of the absolute sign of the quadrupole interaction for the strongly coupled nitrogen atoms and the hyperfine tensor for a mixed $3d_{z^2}$, $3d_{xy}$ SOMO, and spin density plots in DFT calculations with the aim to investigate the binding of H_2. This material is available free of charge via the Internet at http://pubs.acs.org.

IC801383X

(62) Clementi, E.; Raimondi, D. L. *J. Chem. Phys.* **1963**, *38*, 2686–2689.
(63) Rosicky, F.; Mark, F. *Theor. Chim. Acta* **1979**, *54*, 35–51.
(64) Stenson, P. A.; Board, A.; Marin-Becerra, A.; Blake, A. J.; Davies, E. S.; Wilson, C.; McMaster, J.; Schröder, M. *Chem. Eur. J.* **2008**, *14*, 2564–2576.

Supporting information

I. Crystallographic Information File (CIF) for $[(Ni_2(L)ClO_4)_2(\mu_2\text{-}Cl)_2]^{x+}$

Table S1. Crystal Data and Structure Refinement for $[((\mu_2\text{-}ClO_4)(Ni_2(L))_2(\mu_2\text{-}Cl)]_2^{x+}$

Identification code	ni23ns	
Empirical formula	$C_{48}H_{82}Cl_{16}N_8Ni_4O_{71}S_4$	
Formula weight	2837.5	
Temperature	150(2) K	
Wavelength	0.71073 Å	
Crystal system	Triclinic	
Space group	P-1	
Unit cell dimensions	a = 13.239(2) Å	α = 90.431(2)°
	b = 13.607(2) Å	β = 111.058(2)°
	c = 14.751(2) Å	γ = 90.606(2)°
Volume	2479.5(6) Å	
Z	1	
Density (calculated)	1.912 Mg/m^3	
Absorption coefficient	1.385 mm^{-1}	
F(000)	1460	
Crystal size	0.28 x 0.16 x 0.12 mm^3	
Theta range for data collection	1.78 to 27.51°	
Index ranges	−16<=h<=16, −17<=k<=17, −13<=l<=19	
Reflections collected	15639	
Independent reflections	10919 [R_{int} = 0.034]	
Completeness to theta = 24.96°	95.8 %	
Absorption correction	Semi-empirical from equivalents	
Max. and min. transmission	1.000 and 0.720	
Refinement method	Full-matrix least-squares on F^2	
Data / restraints / parameters	10919 / 278 / 715	
Goodness-of-fit on F^2	1.02	
Final R indicies [I>2σ(I)]	R1 = 0.0588, wR2 = 0.136	
R indices (all data)	R1 = 0.116, wR2 = 0.164	
Largest diff. peak and hole	1.38 and –0.72 e.$Å^{-3}$	

II. Coordinates [Å] of the model for $Ni_2(L1)(MeCN)_2$ used in the DFT calculations.

Ni	0.000000	0.000000	0.000000
S	2.368099	0.000000	-0.078061
C	2.765916	-1.105289	1.291375
C	3.879740	-0.812380	2.128325
C	4.637286	0.443526	2.068501
C	4.353974	-1.813585	3.024567
C	3.742532	-3.089635	3.125486
C	4.295651	-4.150961	4.047126
C	2.610070	-3.333340	2.305667
C	2.095585	-2.358891	1.401008
C	0.881407	-2.742890	0.657399
N	-0.023098	-1.981064	0.085618
C	-1.185520	-2.617675	-0.594060
C	-2.539433	-2.052973	-0.116939
C	-2.829665	-0.595803	-0.529584
N	-1.938662	0.394643	0.138612
H	5.655392	0.380880	2.506374
H	5.237383	-1.592016	3.648995
H	3.601197	-5.010595	4.159481
H	5.258935	-4.554722	3.649251
H	4.518224	-3.744766	5.060358
H	2.108874	-4.314987	2.371191
H	0.701241	-3.839861	0.626732
H	-1.065228	-2.452064	-1.690324
H	-1.151949	-3.718925	-0.424098
H	-2.642189	-2.172334	0.986624
H	-3.336416	-2.686425	-0.571323
H	-2.696543	-0.475893	-1.630748
H	-3.891594	-0.343987	-0.301462
S	0.515289	2.297736	-0.080997
Ni	2.605902	2.081157	0.794978
N	4.287469	1.608784	1.556825
C	-2.474732	1.438030	0.729621
C	-0.461018	2.947072	1.292102
N	2.508528	3.858747	1.477043
C	5.359768	2.654032	1.483496
C	-1.824138	2.552355	1.443080
H	-3.585692	1.488492	0.739868
C	0.071969	3.999011	2.086755
C	1.455278	4.477570	1.974038
C	3.771537	4.655161	1.369724
C	4.943757	3.992475	2.102968
H	5.604704	2.788480	0.401549
H	6.279503	2.267124	1.978209
C	-2.646517	3.275321	2.354617
C	-0.787244	4.691516	2.989341
H	1.615893	5.508576	2.352705
H	4.002053	4.761150	0.281899
H	3.593125	5.680566	1.765622
H	4.710561	3.870393	3.186054
H	5.818395	4.680837	2.044644
C	-2.155060	4.353725	3.138114
H	-3.708236	2.987706	2.453518
H	-0.375480	5.527660	3.580798
C	-3.065682	5.123920	4.065049
H	-2.498807	5.801134	4.738579
H	-3.777635	5.757776	3.481633
H	-3.687033	4.445719	4.693526
N	0.000000	0.000000	-2.099999
C	0.046552	0.117859	-3.276803

C	0.119352	0.257949	-4.724206
H	-0.332641	-0.625032	-5.232856
H	1.179685	0.342938	-5.057779
H	-0.425997	1.169905	-5.061243
N	0.023736	0.001550	2.099865
C	-0.148528	-0.183277	3.256048
C	-0.366953	-0.413751	4.679351
H	0.272934	0.258413	5.295998
H	-0.125314	-1.467114	4.951066
H	-1.430928	-0.225550	4.952521

III. The absolute sign of the nuclear quadrupole splitting

The absolute sign of the quadrupole interaction can be determined for the strongly coupled MeCN nitrogen atoms. Consider the intensity distribution of the signals in the ENDOR spectra recorded at the low-field (g_{eff} = 2.210) edge of the EPR spectrum, cf. figure 5. Without hyperfine semi-selection, four bands with about equal intensity are expected, as is shown in the simulation of figure 5. However, when the energy level diagram for an S = ½ system coupled to a nitrogen (I(^{14}N) = 1) with dominant hyperfine interaction is considered (see figure S1), only the ($\Delta M_S = \pm 1$, $M_I = +1$) EPR transition is resonant at the low-field edge of the EPR spectrum. Therefore, in the ENDOR spectrum, the transitions $M_I = 0 \leftrightarrow +1$, indicated in red in figure S1 will dominate and the transitions $M_I = 0 \leftrightarrow -1$ will be attenuated. This is the case for the two innermost signals in the ENDOR spectrum, and such a pattern can only be reproduced by taking a positive value for P_x in Figure S1. If P_x is negative, the outermost two signals will dominate the ENDOR spectrum. By the same arguments, the transitions $M_I = 0 \leftrightarrow -1$ will dominate the ENDOR spectrum for the magnetic field set near g_z (see Figure S1). Since the ENDOR spectrum at g_{eff} = 2.037 displays four signals for which the innermost two dominate the spectrum, P_z has to be negative.

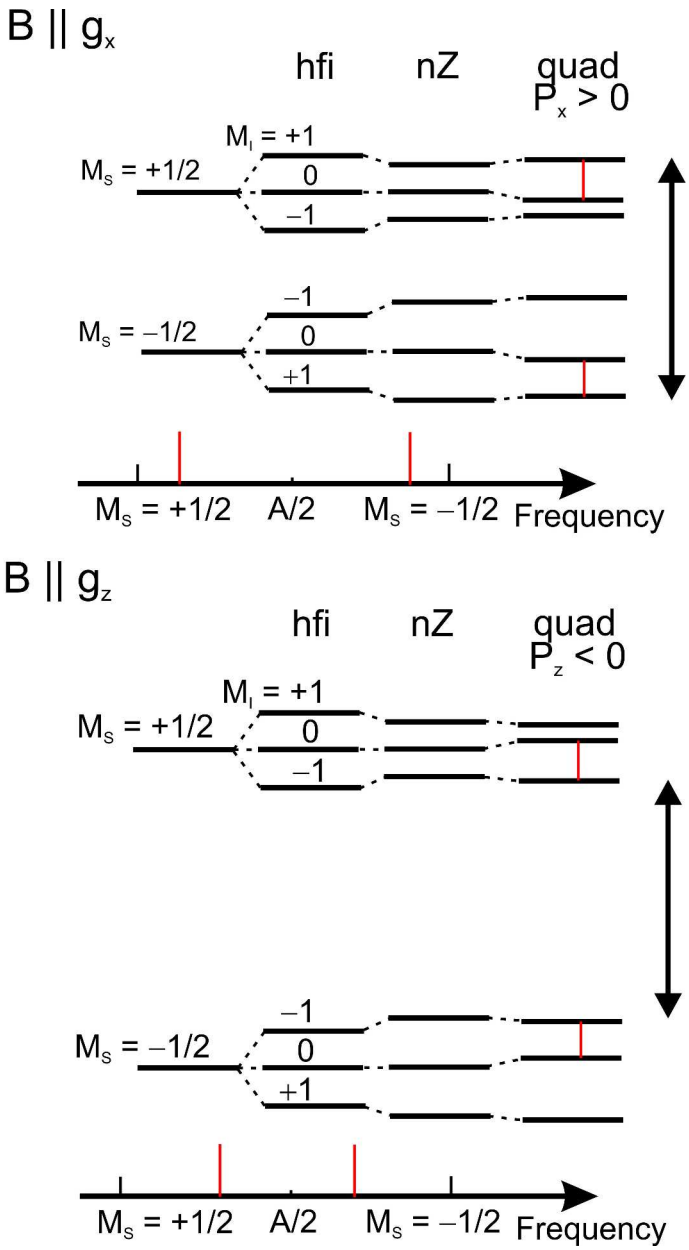

Figure S1. Energy level diagram, including electron and nuclear Zeeman, hyperfine and quadrupole interactions (not to scale) of the electron and nitrogen nuclear spin levels at low-field ($B \parallel g_x$) and high-field ($B \parallel g_z$) edge of the EPR spectrum. The vertical arrow indicates the microwave transition. At both edges, hyperfine-(semi)selection occurs and the two innermost signals in the ENDOR spectrum become dominant only for $P_x > 0$ MHz and $P_z < 0$ MHz.

IV. Hyperfine tensor for a mixed $3d_{z^2}$, $3d_{xy}$ SOMO

IV.1. Definitions

The SOMO as found in $[Ni_2L(MeCN)_2]^{3+}$ is given by

$$\left|\Psi\right\rangle = A\left|xy\right\rangle + E\left|z^2\right\rangle \tag{1.1}$$

where A and E are the wavefunction coefficients. A^2 and E^2 are spin densities in the xy and z^2 orbitals.

General Slater orbital ($n = 3$) expressions for the $3d_{xy}$ and $3d_{z^2}$ orbitals

$$\left|xy\right\rangle = N_{xy}\,xy\,e^{-\zeta r/na_0} = 2\sqrt{\frac{\left(\zeta/a_0\right)^7}{2\pi(3)^8}}\,xy\,e^{-\zeta r/na_0} \tag{1.2}$$

$$\left|z^2\right\rangle = N_{z^2}\left(3z^2 - r^2\right)e^{-\zeta r/na_0} = \sqrt{\frac{\left(\zeta/a_0\right)^7}{2\pi(3)^9}}\left(3z^2 - r^2\right)e^{-\zeta r/na_0} \tag{1.3}$$

where ζ is the Slater exponent and N_{xy} and N_{z^2} are the normalization factors.

The anisotropic hyperfine interaction (see, e.g. Carrington, A. and McLachlan, A.D., "Introduction to magnetic resonance", Harper and Row, New York, 1967) is given by

$$\vec{\vec{A}}(\vec{r}) = -\gamma_e\gamma_N\begin{Bmatrix} r^2 - 3x^2 & -3xy & -3xz \\ -3xy & r^2 - 3y^2 & -3yz \\ -3xz & -3yz & r^2 - 3z^2 \end{Bmatrix}\frac{1}{r^5} \tag{1.4}$$

where γ_e and γ_N are the electronic and nuclear gyromagnetic ratios. Note that the trace of (1.4) is zero.

The hyperfine tensor of the spin Hamiltonian is given by

$$\vec{\vec{A}} = \left\langle\Psi\left|\vec{\vec{A}}(\vec{r})\right|\Psi\right\rangle \tag{1.5}$$

IV.2. Hyperfine tensor for a pure $3d_{z^2}$ SOMO ($A = 0$)

For a pure $3d_{z^2}$ SOMO, equation (1.5) becomes

$$\vec{\vec{A}} = E^2 \left\langle z^2 \left| \vec{\vec{A}}(\vec{r}) \right| z^2 \right\rangle \tag{2.1}$$

The off-diagonal elements are uneven functions of x, y and/or z. Since the $3d_{z^2}$ orbital (1.3) is an even function of x, y and z, all off diagonal elements evaluate to 0. The A_{zz} term evaluates to

$$A_{zz} = -\gamma_e \gamma_N E^2 N_{z^2}^2 \left\langle \left(3z^2 - r^2\right)^2 e^{-2\zeta r/na_0} \frac{r^2 - 3z^2}{r^5} \right\rangle \tag{2.2}$$

The integral can be evaluated after transformation into spherical coordinates

$$A_{zz} = -\gamma_e \gamma_N E^2 N_{z^2}^2 \int dr r^3 e^{-2\zeta r/na_0} \int \sin\theta d\theta \int d\varphi \left(3\cos^2\theta - 1\right)^2 \left(1 - 3\cos^2\theta\right) \tag{2.3}$$

All three integrals are trivial. The φ integration gives 2π. The θ integral can be rewritten as

$$\int_{-1}^{1} dx \left(1 - 3x^2\right)^3 = \frac{-96}{105} \tag{2.4}$$

The r integral evaluates to

$$\int dr r^3 e^{-2\zeta r/na_0} = -\left(\frac{na_0}{2}\right)^3 \frac{\partial^3}{\partial \zeta^3} \int dr e^{-2\zeta r/na_0} = -\left(\frac{na_0}{2}\right)^4 \frac{\partial^3}{\partial \zeta^3}\left(\frac{1}{\zeta}\right) = 6\left(\frac{na_0}{2\zeta}\right)^4 \equiv P_r \tag{2.5}$$

where the r integral is abbreviated as P_r to save space in the coming formulas. Substitution of the integrals into (1.8) gives

$$A_{zz} = -\gamma_e \gamma_N E^2 \frac{\left(\zeta/a_0\right)^7}{2\pi(3)^9} P_r 2\pi \frac{-96}{105} = \gamma_e \gamma_N E^2 P_r \frac{\left(\zeta/a_0\right)^7}{(3)^8} \frac{32}{105} \tag{2.6}$$

The A_{xx} and A_{yy} elements can in principle be calculated similarly. However, it is known that the trace of the anisotropic tensor (1.4) is 0 ($A_{xx} + A_{yy} + A_{zz} = 0$) and it is trivial to see that the A_{xx} and A_{yy} terms give exactly the same integral. Thus, $A_{xx} = A_{yy} = -½A_{zz}$. The total hyperfine tensor for a pure $3d_{z^2}$ SOMO becomes

$$\vec{\vec{A}} = \gamma_e \gamma_N E^2 P_r \frac{\left(\zeta/a_0\right)^7}{(3)^8} \frac{32}{105} \begin{pmatrix} -\frac{1}{2} & 0 & 0 \\ 0 & -\frac{1}{2} & 0 \\ 0 & 0 & 1 \end{pmatrix} \tag{2.7}$$

The tensor is axial and colinear with the xyz axes of the set of d orbitals.

IV.3. Hyperfine tensor for a pure $3d_{xy}$ SOMO ($E = 0$)

Now we derive the hyperfine tensor in the case of a pure $3d_{xy}$ orbital. Equation (1.5) evaluates to

$$\vec{\vec{A}} = A^2 \left\langle xy \left| \vec{\vec{A}}(\vec{r}) \right| xy \right\rangle \tag{3.1}$$

The off diagonal elements are again zero, because the integrand is an uneven function of *x*, *y* and/or *z*. The A_{zz} element becomes

$$A_{zz} = -\gamma_e \gamma_N A^2 N_{xy}^2 \left\langle x^2 y^2 e^{-2\zeta/na_0} \frac{r^2 - 3z^2}{r^5} \right\rangle \tag{3.2}$$

Transformation into spherical coordinates leads to

$$A_{zz} = -\gamma_e \gamma_N A^2 N_{xy}^2 \int dr r^3 e^{-2\zeta r/na_0} \int \sin\theta d\theta \int d\varphi \sin^4\theta \sin^2\varphi \cos^2\varphi \left(1 - 3\cos^2\theta\right) \tag{3.3}$$

The r integral is equal to (2.5) and the φ integral evaluates as

$$\int_0^{2\pi} d\varphi \sin^2\varphi \cos^2\varphi = \frac{\pi}{4} \tag{3.4}$$

The θ integral simplifies to

$$\int_{-1}^{1} dx \left(1 - x^2\right)^2 \left(1 - 3x^2\right) = \frac{64}{105} \tag{3.5}$$

Substitution of the integrals into (3.3) followed by normalization gives

$$A_{zz} = -\gamma_e \gamma_N A^2 4 \frac{\left(\zeta/a_0\right)^7}{2\pi(3)^8} P_r \frac{16\pi}{105} = -\gamma_e \gamma_N A^2 \frac{\left(\zeta/a_0\right)^7}{(3)^8} P_r \frac{32}{105} \tag{3.6}$$

Note that except for the − sign, the expression (3.6) equals (2.6). The A_{xx} and A_{yy} elements are again either evaluated similarly, or by making use of the tracelessness of (1.4). Thus, $A_{xx} = A_{yy} = -\frac{1}{2}A_{zz}$. The total hyperfine tensor for a pure $3d_{xy}$ SOMO is

$$\vec{\vec{A}} = -\gamma_e \gamma_N A^2 P_r \frac{\left(\zeta/a_0\right)^7}{(3)^8} \frac{32}{105} \begin{pmatrix} -\frac{1}{2} & 0 & 0 \\ 0 & -\frac{1}{2} & 0 \\ 0 & 0 & 1 \end{pmatrix} \tag{3.7}$$

The expressions (2.7) and (3.7) only differ in sign, and the coefficients A^2 and E^2. The tensor is again axial and colinear with the *xyz* axes of the set of d orbitals.

IV.4. Hyperfine tensor for mixed $3d_{z^2}$, $3d_{xy}$ SOMO

Following the same procedure again and using (1.1) as the SOMO, equation (1.5) becomes

$$\vec{\vec{A}} = E^2\left\langle z^2 \left|\vec{\vec{A}}(\vec{r})\right| z^2\right\rangle + A^2\left\langle xy\left|\vec{\vec{A}}(\vec{r})\right| xy\right\rangle + 2AE\left\langle xy\left|\vec{\vec{A}}(\vec{r})\right| z^2\right\rangle \tag{4.1}$$

The first two terms have been evaluated in sections 2 and 3. The cross term $2AE\left\langle xy\left|\vec{\vec{A}}(\vec{r})\right| z^2\right\rangle$ now has to be evaluated. The cross term only contributes to the A_{xy} element of (1.4), since all other elements give an integrand that is uneven with respect to either *x*, *y* or *z*. The A_{xy} element becomes

$$A_{zz} = -\gamma_e\gamma_N 2AEN_{xy}N_{z^2}\left\langle xy\left(3z^2 - r^2\right)e^{-2\zeta/na_0}\frac{-3xy}{r^5}\right\rangle \tag{4.2}$$

Transformation into spherical coordinates gives

$$\begin{aligned} A_{zz} &= -\gamma_e\gamma_N 2AEN_{xy}N_{z^2}\int dr r^3 e^{-2\zeta r/na_0}\int \sin\theta d\theta\int d\varphi(-3)\sin^4\theta\sin^2\varphi\cos^2\varphi\left(3\cos^2\theta - 1\right) \\ &= \gamma_e\gamma_N 6AEN_{xy}N_{z^2}P_r\int \sin\theta d\theta\int d\varphi\sin^4\theta\sin^2\varphi\cos^2\varphi\left(3\cos^2\theta - 1\right) \end{aligned} \tag{4.3}$$

The θ and φ integrals equal (3.4) and minus (3.5). Thus,

$$\begin{aligned} A_{zz} &= \gamma_e\gamma_N 6AEN_{xy}N_{z^2}P_r\frac{\pi}{4}\left(-\frac{64}{105}\right) = \gamma_e\gamma_N 6AEP_r\frac{2}{\sqrt{3}}\frac{\left(\zeta/a_0\right)^7}{2\pi(3)^8}\frac{\pi}{4}\left(-\frac{64}{105}\right) \\ &= -\gamma_e\gamma_N AEP_r\sqrt{3}\frac{\left(\zeta/a_0\right)^7}{(3)^8}\frac{32}{105} \end{aligned} \tag{4.4}$$

The total hyperfine tensor becomes

$$\vec{\vec{A}} = -\gamma_e\gamma_N P_r\frac{\left(\zeta/a_0\right)^7}{(3)^8}\frac{32}{105}\begin{pmatrix} -\frac{1}{2}\left(A^2 - E^2\right) & \sqrt{3}AE & 0 \\ \sqrt{3}AE & -\frac{1}{2}\left(A^2 - E^2\right) & 0 \\ 0 & 0 & \left(A^2 - E^2\right) \end{pmatrix} \tag{4.5}$$

Thus, the cross term of (4.1) causes a reorientation of the principal *x* and *y* axes of $\vec{\vec{A}}$. The principal *z* axis remains parallel to the *z* axis of the $3d_{z^2}$ orbital. Diagonalization of (4.5) gives eigenvalues (denoted by primes)

$$\begin{cases} A'_x = -\gamma_e \gamma_N P_r \dfrac{\left(\zeta/a_0\right)^7}{(3)^8} \dfrac{32}{105}\left[-\dfrac{1}{2}\left(A^2 - E^2\right) + \sqrt{3}AE\right] \\ A'_y = -\gamma_e \gamma_N P_r \dfrac{\left(\zeta/a_0\right)^7}{(3)^8} \dfrac{32}{105}\left[-\dfrac{1}{2}\left(A^2 - E^2\right) - \sqrt{3}AE\right] \\ A'_z = -\gamma_e \gamma_N P_r \dfrac{\left(\zeta/a_0\right)^7}{(3)^8} \dfrac{32}{105}\left(A^2 - E^2\right) \end{cases} \tag{4.6}$$

In general, the additional terms cause rhombicity, i.e., A'_x and A'_y are no longer equal. However, for the case $A = \pm\sqrt{3}E$ and $E = \pm\sqrt{3}A$, the tensor becomes axial.

V. Structures (left) and spin density plots (right) in DFT calculations with the aim to investigate the binding of H_2.

V.1. $[Ni_2(L)(MeCN)(H_2)]^{3+}$

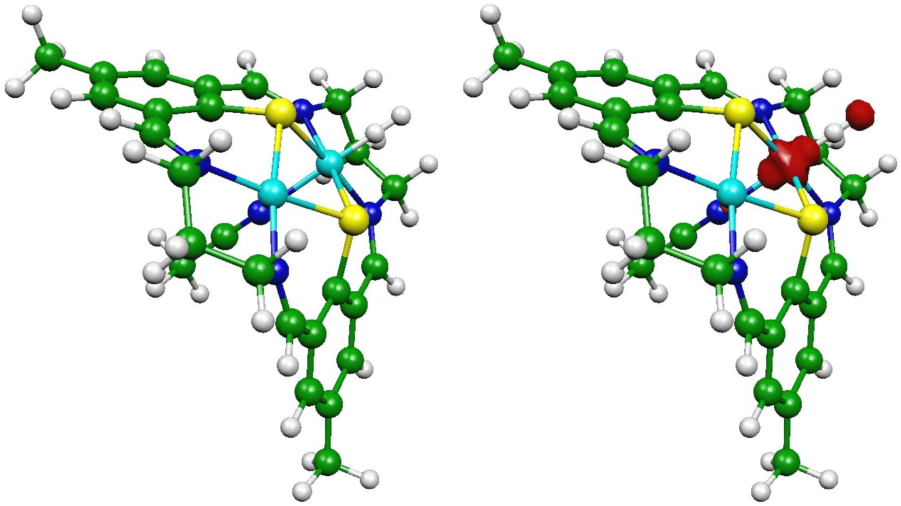

V.2 $[Ni^{3+}(SH^-)_4(OH^-)(H_2)]$

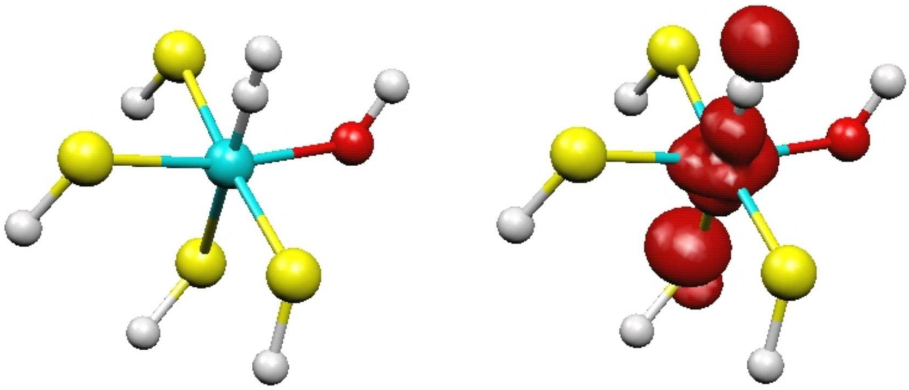

V.3 Hydrogenase active site, $[Fe^{2+}(CN^-)_2(CO)Ni^{3+}(SCH_2CH_3^-)_4(OH^-)(C_4NH_3CH_3)(H_2)]$